Single-shot multispectral quantitative phase imaging of biological samples using deep learning

SUNIL BHATT,[1,†,*] ANKIT BUTOLA,[2,†] ANAND KUMAR,[1] PRAMILA THAPA,[1] AKSHAY JOSHI,[3] SUYOG JADHAV,[4] NEETU SINGH,[3] DILIP K. PRASAD,[4] KRISHNA AGARWAL,[2] AND DALIP SINGH MEHTA[1,#]

[1]*Bio-photonics and Green-photonics Laboratory, Department of Physics, Indian Institute of Technology Delhi, Hauz-Khas, New Delhi 110016, India.*
[2]*Department of Physics and Technology, UiT The Arctic University of Norway, 9037 Tromsø, Norway.*
[3] *Centre for Biomedical Engineering, Indian Institute of Technology Delhi, Hauz-Khas, New Delhi 110016, India.*
[4]*Department of Computer Science, UiT The Arctic University of Norway, 9037 Tromsø, Norway.*
[#] *Dalip.Singh.Mehta@physics.iitd.ac.in*
†Shared first authors
** sunilbhatt.619@gmail.com*

Abstract: Multi-spectral quantitative phase imaging (MS-QPI) is a label-free technique to determine the morphological changes, refractive index variations, and spectroscopic information of the specimens. The bottleneck to implementing this technique to extract quantitative information is the need for more than two measurements for generating MS-QPI images. We propose a single-shot MS-QPI technique using a highly spatially sensitive digital holographic microscope (DHM) assisted by a deep neural network (DNN). There are three different wavelengths used in our method: λ=532, 633, and 808 nm. The first step is to get the interferometric data for each wavelength. The acquired datasets are used to train a generative adversarial network (GAN) to generate multi-spectral quantitative phase maps from a single input interferogram. The network was trained and validated on two different samples: the optical waveguide and MG63 osteosarcoma cells. Validation of the present approach is performed by comparing the predicted multi-spectral phase maps with numerically reconstructed (FT+TIE) phase maps and quantify with different image quality assessment metrices.

1. Introduction

Quantitative phase imaging (QPI) is a prominent label-free technique to measure morphological changes of biological cells that are transparent in nature[1-3]. Over the last few decades, QPI has been evolved both experimentally and computationally to resolve complexity of system and reconstruction for the accurate measurement and classification of various parameters of biological cells and tissues, such as surface profile, refractive index, dry mass density, cell membrane fluctuations, among others[4-12]. In QPI, morphological and dynamical information about the samples can be extracted by measuring the path length shift ($\Delta\phi$) associated with the objects, which contains information about the refractive index (n_s) and thickness (d) of the specimens. For the improvement in the specificity of QPI, image acquisition with additional dimensions of measurements, such as sample rotation, angle, and wavelength, is required, which results in 3D QPI[13, 14].

In addition, a number of optical properties such as absorption, scattering, reflection, refractive index, phase (coupled information of refractive index and thickness), etc. in a cell or tissue which are wavelength dependent and affect the diagnostic applications [15]. The ability of light to penetrate, interact, and transmit the cell or tissue organelles is the key to diagnosis, and mainly depend on the cell's morphology and variation of refractive index and thickness inside the cell or tissue. Thus, a technique which can provide refractive index and thickness variation inside the cells or tissues is essential to increase the accuracy of diagnosis. Multispectral

quantitative phase imaging (MS-QPI) is such an imaging technique used for the quantitative analysis of phases that depend on a cell's refractive index and thickness.

In the past, different methods such as diffraction phase microscopy [16, 17], quantitative dispersion microscopy[18] , quantitative phase spectroscopy[19], and dynamic spectroscopic phase microscopy[20], swept-source diffraction phase microscopy [21] etc. have been developed for phase measurement at multiple wavelengths. These methods have been utilised to overcome issues such as phase noise, phase unwrapping, and determination of refractive index dependence on the illumination wavelength. The acquisition of such multi-spectral (MS)-QPIs can be done either in a) sequential mode [22-25] i.e., multi-wavelength frames are recorded one after another by wavelength switching or b) in simultaneous mode [26-28] i.e., single frame recorded on a multi-chip color camera which digitally separates out later. The conventional MS-QPI's have certain limitations and complications as per optics perspective, that are mainly.

1. In sequential illumination mode, firstly a costly wavelength switching light source with additional optical component is required [29], that makes system costly and bulky. Secondly, multiple frames corresponding to individual wavelength are recorded either by manual or mechanical switching of the light source that makes system complex and time consuming.
2. On the other hand, in simultaneous illumination mode, a multiwavelength broadband light source with dispersion compensation mechanism and high-cost multi-chip color camera or multiple single-chip cameras are required, which results in complex system with color cross talk problem [23, 26, 30-32].
3. In addition, microbiological organelles are more reliable for imaging in NIR-IR wavelength range. Since in the UV or visible spectral range, some proteins such as hemoglobin (Hb), hemoglobin dioxide (HbO_2), etc. inside the cells or tissues absorb lower wavelength lights more[33-36]. On the contrary, the water and lipids inside the cells or tissues absorb higher wavelength light radiation more [33-35]. Thus, the intermediate optimized condition for imaging with less damage and high penetration is in NIR-IR range (800-1100 nm) for the biological cells or tissues. The traditional MSQPI systems are limited for visible light spectrum (400-700 nm) range. The wide spectral source containing visible-NIR wavelength range require high-cost source and visible-IR sensitive cameras for data acquisition in traditional MSQPI that makes system bulky and costly.

Thus, a technique is required which overcomes these aforementioned limitations with significant time reduction and precision, we have proposed the idea of single-shot MS-QPI assisted with DNN to extract out multispectral parameters.

In the current study, we present a single-shot MS-QPI technique assisted by a deep neural network (DNN) to extract multispectral phase images of industrial and biological samples. For this purpose, we used a partially spatially coherent (PSC) light-based digital holographic microscopy (DHM) system to obtain multi-spectral phase maps from a single input interferogram. The interferometric images are acquired using the Linnik interferometer sequentially by wavelength switching and processed for the extraction of phase maps of the sample for each wavelength, respectively. These phase maps are used to train the generative adversarial network (GAN). We used two different classes of samples for our proposed work: 1) optical waveguide as an industrial sample and 2) MG 63 osteosarcoma cells as a biological sample. The reason for choosing two different classes of samples is to train and test the network with both homogeneous and heterogeneous sample configurations. For this, we apply the concept to a more controlled homogeneous sample, such as an industrial sample whose geometry and configuration are fixed, and to an inhomogeneous sample, such as a

biological sample whose shape is not fixed and changes depending on the sample's position and refractive index. Initially, for the validation of our approach, we used only two wavelength datasets for the optical waveguide, i.e., green and red. The reason to choose only two wavelengths for the optical waveguide is to check how network trained and performs for a simple homogeneous sample. After successful adaptation of the network with two wavelengths for the optical waveguide, we have used three wavelengths, i.e., green, red, and NIR, for the biological sample. The phase maps retrieved from the experimentally recorded interferograms for both the samples are compared with the trained GAN generated phase maps to evaluate the performance of the network. Therefore, our framework performs both phase reconstruction from interferogram and multi-spectral estimation in an integrated manner without resorting to the conventional reconstruction approach. This implies that our network learns the physics of reconstruction and encodes the spectral properties of piece-wise homogeneous materials in the overall inhomogeneous samples. In addition, in the proposed study, by overcompensating the usual requirement of traditional MS-QPI methods we aimed the significant time reduction along with cost and experimental system management. Indeed, it assumes that the training dataset has sufficient representatives of the structural and spectral variation expected in the sample. However, it reduces the experimental and computational demands of performing MS-QPI in the conventional manner.

2. Experimental Setup

The experimental setup of the proposed framework to acquire the single-shot MS-QPI is shown in Fig. 1. Lasers can't be used directly for MS-QPI because speckles and reflections from multiple layers of the sample or the optical components produce spurious and parasitic fringes that don't belong to the sample[25, 37, 38]. These speckles and spurious fringes reduce the resolution as well as the features of the reconstructed phase maps[25, 39]. Therefore, we realise a partially spatially coherent (PSC) light source, i.e., temporally high but spatially low coherent, by passing the laser light through a rotating diffuser (RD) and a multi-multimode fibre bundle (MMFB). The multi-multimode fibre bundle (MMFB) is made up of N∼6400 multimode fibres having a core diameter of ∼50μm of each with a numerical aperture of 0.65 (Wuzhou Aokace Technology Co., Ltd). The length and the active diameter of MMFB is 1.8m and 4mm, respectively. The RD scatters photons into various directions and creates a temporally narrow and wide angular spectral source, which is further coupled into the input of the MMFB. Spatial, temporal, and angular diversity can help reduce the speckles of coherent laser light sources [39].

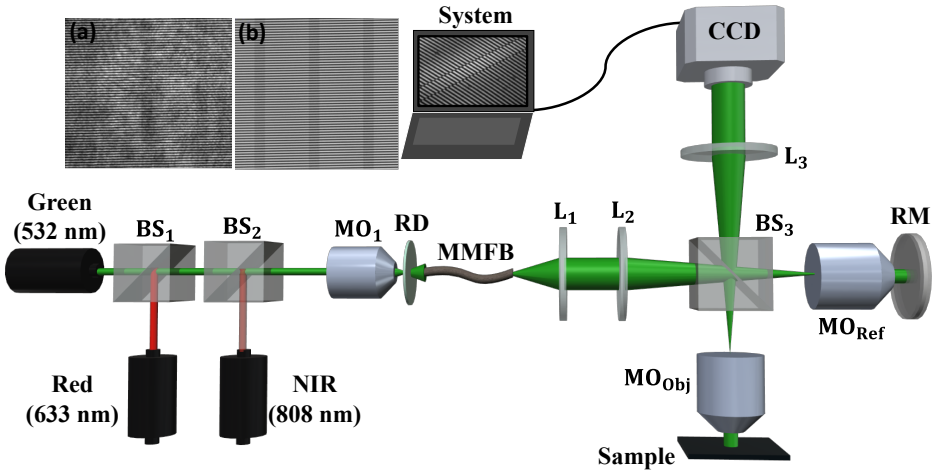

Fig. 1. The multispectral quantitative phase imaging (MS-QPI) system is depicted schematically. Three different LASERs were used (green DPSS (λ=532 nm), He-Ne (λ=633 nm), and near infrared (λ=808 nm).BS_1, BS_2 and BS_3:

beam splitter; MO: microscopic objectives (10X, 0.25 NA); RD: rotating diffuser; MMFB: multi multimode fibre bundle; L_1, L_2 and L_3: lenses; RM: reference mirror; CCD: charge-coupled device (INFINITY2, Lumenera). (a) speckled interferogram due to high spatial coherence of direct laser illumination. (b) interferogram without speckles using partially spatial coherent light source.

Here, we use laser light sources of three different wavelength, namely green (DPSS, λ_1= 532 nm), red (He-Ne laser, λ_2= 633 nm), and NIR (laser diode dot module, λ_3= 808 nm). For speckle free imaging, these sources are sequentially passed through a microscopic objective (MO_1), RD, and MMFB. The light from the MMFB is coupled at the input port of the Linnik interferometer. The output beam from MMFB is collected by the lens L_1 which is first collimated and then focused by lens L_2 into the back focal plane of two identical microscope objectives, MO_{obj} (sample arm) and MO_{ref} (reference arm) by using the 50/50 beam splitter (BS_3). The focused light is passed through the MO_{obj} which uniformly illuminates the sample. The back reflected light beam from the sample that holds the sample information interferes with the reference beam at the beam splitter plane. The interference signal is further collimated and projected into the charged coupled device (INFINITY2, Lumenera) camera plane using the tube lens L_3.

Further, the light sources are switched to record multi-wavelength interferograms, which are used for phase reconstruction of the sample using the Fourier transform (FT) algorithm. The reason to choose FT over other phase reconstruction algorithm such as phase-shifting is its single frame requirement for reconstruction that comparatively limits the data acquisition in our proposed work. The mathematics and detailed discussion about the FT reconstruction is provided in **Supplementary Note 1** of the **supplement file 2.** The unwrapping (continuous) of the phase map is incorporated by applying the transport of intensity equation (TIE) algorithm[40, 41]. The TIE approach is fast and simpler for the biological cells and tissues as compared to the other unwrapping methods in QPI. The high fringe density interferograms at the camera plane are achieved by tilting the reference mirror (RM). The approach of this study is to generate simultaneous multi-spectral phase maps from a single input interferogram. To achieve this purpose, we train a generative adversarial network (GAN), which is basically a DNN for the execution of the study. In our proposed study, we were using three different wavelength light sources thus, 3X time is required for one set of data acquisition with sequential switching. After training of the proposed MSQPI+DNN framework, no further data acquisition required anymore thus, comparatively the time reduction will be expected more than 3-fold than the traditional acquisition time.

3. The Architecture of Generative Adversarial Network (GAN)

GAN is made up of two models: Generator (G) and Discriminator (D)[42]. The generator generates some mapped images G (I_R), which are then compared to the ground truth (target) images by the discriminator. Ground truth (GT) images are final output images that have been experimentally processed and then sent into the network for training. The training of these two models and the training datasets determines GAN's overall performance. An increase in the number of training datasets leads to improved network training. GAN's architecture is depicted in Fig. 2. In Fig. 2 (a), (b), we showed the U-net architecture of the generator[42, 43], which comprises encoders and decoders, and the PatchGAN architecture of the discriminator, respectively [42, 44].

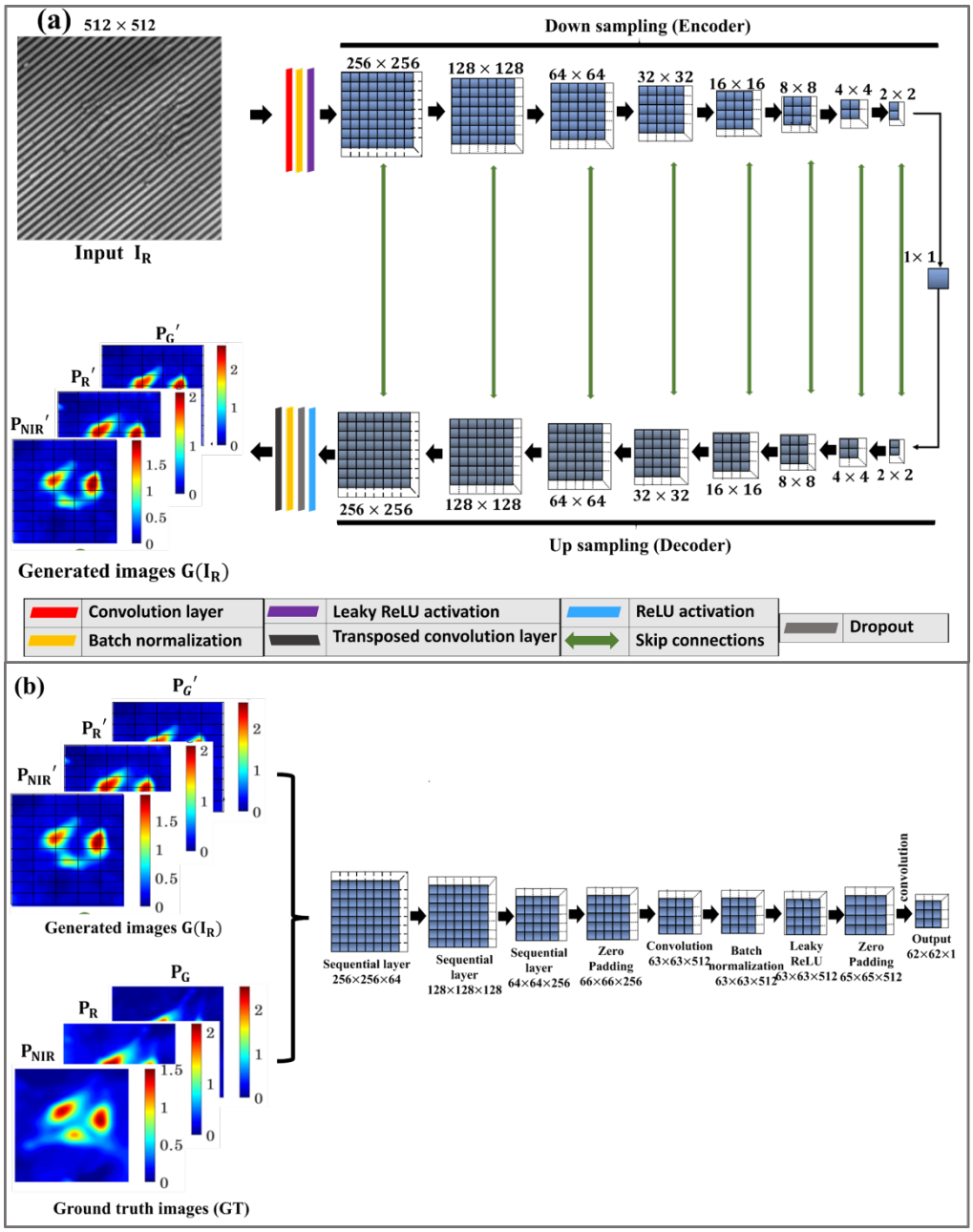

Fig. 2. The architecture of a generative adversarial network (GAN) to generate multispectral quantitative phase images. (a) architecture of generator (G), (b) architecture of discriminator (D).

In the present study, the generator takes a single interferogram as an input I_R, while the discriminator takes generated phase maps from the generator ($G(I_R)$) along with ground truth (GT) as shown in Fig. 2 (a) and (b). The function of the discriminator is to discriminate between the generated and the ground truth images [45]. At the time of training, network optimises the losses between the generated and ground truth images after each epoch. The upgraded loss is then fed back into the generator and discriminator for fine tuning of the network. The detailed information about the working of GAN can be found in the **supplement 1.**

4. Cell culturing process of MG63 osteosarcoma cells:

The preparation of MG63 osteosarcoma cells was carried out at the Centre for Biomedical Engineering, IIT Delhi, India, and the optical waveguide was developed at UiT, The Arctic University of Norway. The MG63 osteosarcoma cells are malignant bone cancer cells with abnormalities in their cellular structure. The cells were cultured using high-glucose DMEM media with 10% fetal bovine serum (FBS) and 1% antibiotic antimycotic solution and incubated in a humidified atmosphere containing 95% air and 5% CO_2 at 37°C. Before seeding, silicon wafers were sterilised using UV and ethanol treatments for 10 min each. Cells were seeded on a sterilised silicon wafer in a 24 well plate and incubated for more than 48 hours in a CO_2 incubator. Later, the samples were washed gently with phosphate-buffered saline (PBS) and fixed with 4% paraformaldehyde. To perform the experiment, PBS-dipped cells were placed under the proposed MS-QPI system for data recording.

5. Workflow of the framework: Data acquisition, network training, and network testing

The workflow of the present MS-QPI+DNN framework for the generation of simultaneous multispectral phase maps from a single input interferogram (i.e., single-shot MS-QPI) is shown in Fig. 3. The current framework is made up of three parts: data acquisition and processing, training, and testing of the network itself.

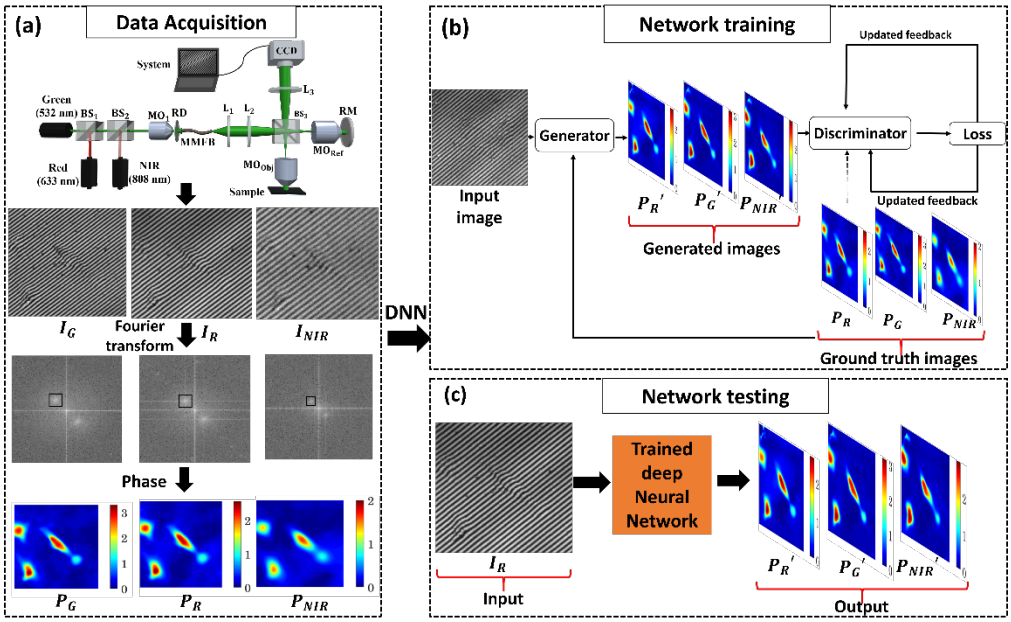

Fig. 3. Workflow of the MS-QPI+DNN framework: (a) data acquisition process where IG, IR, INIR, and PG, PR, PNIR, are the three wavelength interferograms and their corresponding phase maps for λ=532 nm (green), λ = 633nm (red), and λ=808nm (NIR), respectively using MS-QPI system. (b) block diagram for the training process of DNN. (c) block diagram of network testing for multispectral phase map generation.

During data acquisition, we recorded multi-spectral interferograms by switching the light sources as shown in Fig. 3 (a). The optical waveguide and MG63 cell data were acquired using the MS-QPI system by employing two identical microscope objectives (MO_{obj} = MO_{ref}). For the experimentation we have used a planar strip waveguide of Ta2O5 (ncore=2.1) guiding layer having thickness of 4-220 nm etched over SiO2 and Si (n=1.45) with varying strip width of 1.3µm-200µm. The recorded interferometric images of samples were reconstructed using the

Fourier transform (FT) and the TIE unwrapping algorithm. As shown in Fig. 3 (b), we trained the network using a single input interferogram and three phase maps (ground truth images) corresponding to different 'λ_i'. During training, a single interferogram was taken as an input to the generator to generate some mapped images. The discriminator discriminates between the generated and ground truth images and calculates a loss which can be fed back to the generator and discriminator for fine tuning of the network. After several iterations, the generator had enough training to generate the same images as the ground truth, i.e., loss reaches a minimum. As shown in Fig. 3, (c), the trained network was used for testing. Although, for network training, multiple interferometric images corresponding to each wavelength is required. But, after successful training of the network, multi wavelength interferograms are not required to predict the multispectral phase map of the samples. Interestingly, MS-QPI assisted with deep learning help us to extract multispectral phase information about the sample from a single wavelength interferogram.

The optical waveguide dataset was trained with 54,414,979 trainable parameters in the generator model and 2,768,641 trainable parameters in the discriminator model. The model was trained with 4080 data sets with an input image size of 256×256, batch size 1, and a buffer size of 400 (for data randomization) for the optical waveguide. For complex structures like MG63 cell datasets, a total of 11,556 data items were employed to train the network. For the MG63 cell dataset, 66,999,939 trainable parameters in the generator model and 2,768,641 trainable parameters in the discriminator model were used. This model was trained with an input image size of 512×512, batch size 1, and a buffer size of 400. The optimized epoch was set at 70 by evaluating the training characteristics. The training time used for 100 epochs was 27.76 hours with inference time 108ms ± 26.3ms per run (mean ± std. dev. of 10 runs). We used 80% of total datasets for training and validation, while 20% of the dataset for testing purpose. The network has not reached over-learning during the training we have provided the training and validation vs. epoch curves in the **Supplementary Figure 7** in the **supplement file 2**. The ablation study regarding NN, why we ended up with this net structure and this number of layers is provided in the **Supplementary Note 2** in the **supplement 2**.

The network was programmed in Python (version 3.8.0) and implemented using TensorFlow-GPU (version 2.6) and Keras (version 2.2.0) library functions on an Anaconda Jupyter notebook. Network was trained at NVIDIA DGX-A100 server (AMD EPYC 7742 CPU, NVIDIA A100 40GB GPU) processor.

6. Results and Discussion

In the present work, we have shown the comparison between the experimentally processed phase maps and the network generated results of the optical waveguide and MG63 cell dataset. The network is optimised and trained for both datasets individually. Since the model is trained about the sample's specific properties such as geometry, dry mass, refractive index variation, thickness, and density etc., and these properties vary sample to sample. Thus, the trained network used for multispectral phase map data generation is sample dependent i.e., for multispectral quantitative phase imaging of a new sample, network should be trained from scratch for the accurate mapping of biological parameters.

Figure 4 shows the comparison of numerically (FT+ TIE algorithm based) reconstructed and network generated multispectral phase map data of the optical waveguide. The input interferogram corresponding to λ=633 nm is shown in Fig. 4 (a). Figure 4 (b) and (c) are numerically reconstructed 2D and 3D phase maps corresponding to λ=532 nm and λ=633 nm, respectively, for experimentally recorded interferograms. Figure 4 (d) and (e) are the network generated 2D and 3D phase maps corresponding to λ=532 nm and λ=633 nm, respectively, from a single input interferogram. The comparison shows that there is a wavelength dependent phase

map variation predicted by the network that is similar to the experimental reconstructed phase maps. Since the phase map is inversely proportional to the illumination wavelength, the phase value decreases as the wavelength increases. This is also predicted by the network, which can be seen in through colormap variation that signifies training of the wavelength dependency by the network for phase prediction.

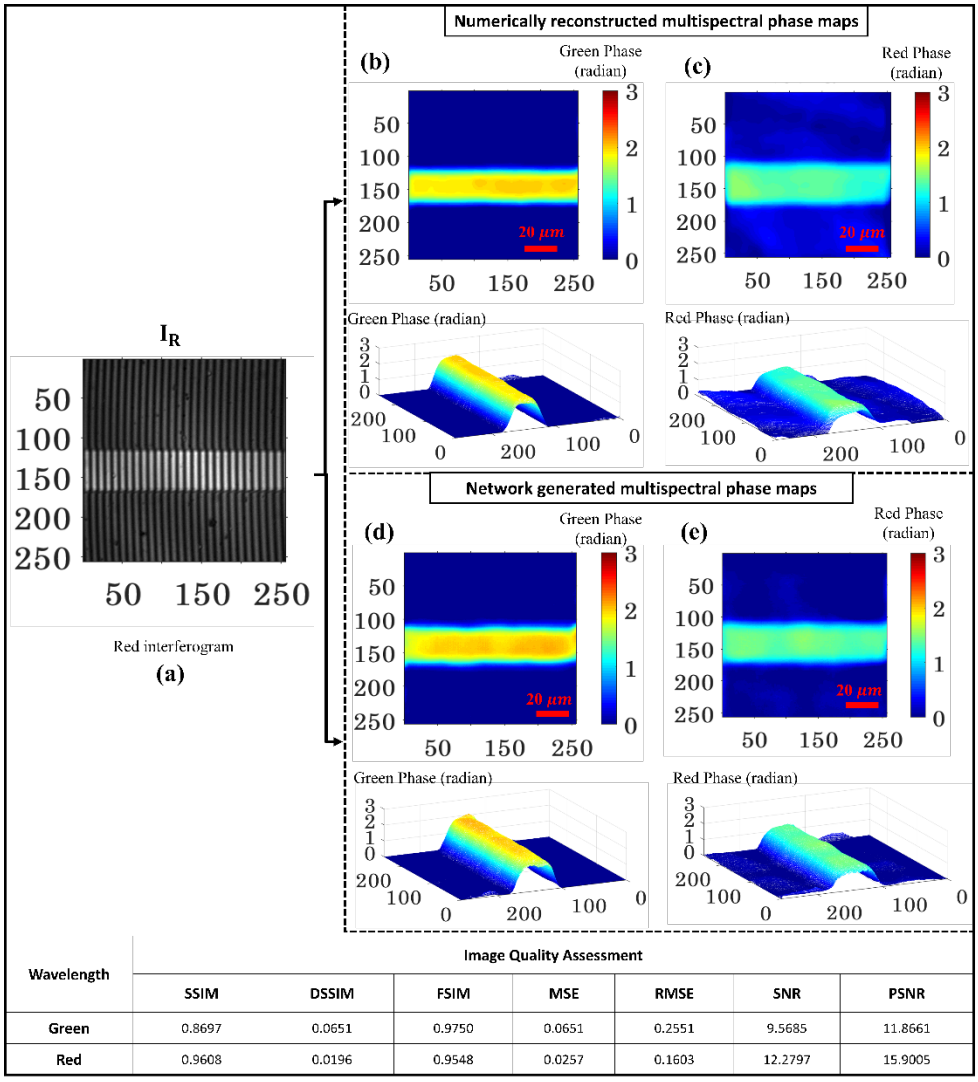

Wavelength	Image Quality Assessment						
	SSIM	DSSIM	FSIM	MSE	RMSE	SNR	PSNR
Green	0.8697	0.0651	0.9750	0.0651	0.2551	9.5685	11.8661
Red	0.9608	0.0196	0.9548	0.0257	0.1603	12.2797	15.9005

Fig. 4. Showing comparison between numerically (FT+ TIE algorithm based) reconstructed and network generated multispectral phase map data generated from a single input hologram on an optical waveguide. (a) is the experimentally recorded input red wavelength interferogram (b), (c) are the numerically reconstructed 2D and 3D phase maps for experimentally recorded green and red wavelength interferograms, respectively. (d), (e) are the network generated 2D and 3D phase maps corresponding to green and red wavelength, respectively. In order to support the robustness of the network for multispectral phase map data generation form a single hologram, image quality assessment between the numerically (FT+ TIE algorithm based) reconstructed and network generated multispectral phase maps is performed. The SSIM, DSSIM, FSIM, MSE, RMSE, SNR, and PSNR value of two images (the numerically reconstructed and network predicted) corresponding to each wavelength are listed in Table in Fig. 4.

In order to quantify the performance of MS-QPI+DNN, we calculated Structure Similarity Index Measure (SSIM) [46, 47], Structural Dissimilarity (DSSIM)[47], Features Similarity Index Matrix (FSIM)[47], Mean Square Error (MSE)[47], Root Mean Square Error (RMSE)[47], Signal-to-Noise Ratio (SNR), and Peak Signal-to-Noise Ratio (PSNR)[47] between numerically reconstructed and network generated phase maps. The SSIM lies [0 1], 0 correspond to least similarity in structure while 1 corresponds to two images are similar to each other. The values for FSIM lies [0 1], maps the features and measures the similarities between two images. The high value of SSIM and FSIM signifies that the similarity in structure between the network generated and numerically reconstructed phase maps is of good resemblance. Hence, the network is well trained for the MS-QPI with higher similarity in structure and feature for multi-spectral data generation. The slight difference in SSIM and FSIM value be caused by network artefacts during data training, such as data conversion, data processing, and so on. In human perception other than SNR and PSNR, SSIM or FSIM provides better results since it is normalized between [0 1], so more understandable than absolute errors like in MSE or PSNR[47]. The errors DSSIM, MSE, and RMSE tending to zero signifies minimum error between the two images and high values of SNR and PSNR signifies better the quality of generated images.

In support of the network performance, the histogram plot of MSE, SSIM and PSNR over the complete test dataset, few more reconstructed results and quantifying parameters are provided in the **Supplementary Figure 1, 2 and 3** on the **Supplement file 2.**

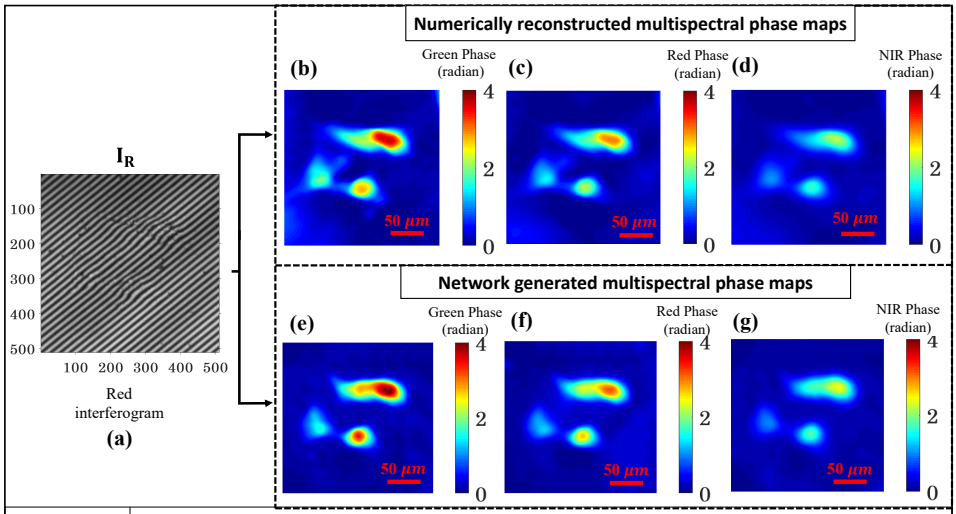

Wavelength	Image Quality Assessment						
	SSIM	DSSIM	FSIM	MSE	RMSE	SNR	PSNR
Green	0.9182	0.0409	0.9568	0.0837	0.2894	10.4873	10.7708
Red	0.9464	0.0268	0.9533	0.0389	0.1973	11.8082	14.0994
NIR	0.9565	0.0217	0.9641	0.0149	0.1221	10.9321	18.2668

Fig. 5. Illustration of comparison between numerically (FT+ TIE algorithm based) reconstructed and network generated multispectral phase map data from a single input interferogram on MG63 osteosarcoma cells. (a) is the experimentally recorded input red wavelength interferogram. (b), (c) and (d) are the numerically reconstructed phase maps for experimentally recorded green, red, and NIR wavelength interferograms, respectively. (e), (f) and (g) are the network-generated multispectral phase maps corresponding to green, red, and NIR wavelengths, respectively. In order to support the robustness of the network for multispectral phase map data generation form a single hologram, image quality assessment between the numerically (FT+ TIE algorithm based) reconstructed and network generated multispectral phase maps is performed. The SSIM, DSSIM, FSIM, MSE, RMSE, SNR, and PSNR value of two images (the numerically reconstructed and network predicted) corresponding to each wavelength are listed in Table in Fig. 5.

Figure 5 shows the comparison of numerically (FT+ TIE algorithm based) reconstructed and network generated multispectral phase map data from a single input interferogram on MG63 cell dataset. The NIR wavelength λ =808 nm is chosen since it has low absorption of biological molecules in this region[48]. Furthermore, NIR imaging is superior for thicker biological samples because it allows the better penetration at low illumination intensities, reducing the risk of photobleaching, achieving improved contrast and resolution, and reducing the possibility of crosstalk between channels. The input interferogram corresponding to λ=633 nm is shown in Fig. 5 (a). Figure 5 (b), (c), and (d) are the numerically reconstructed 2D phase maps corresponding to λ=532 nm, λ=633 nm and λ=808 nm, respectively. Figure 5 (e), (f), and (g) are the network-generated 2D phase maps that correspond to λ=532 nm, λ=633 nm, and λ=808 nm, respectively. The comparison shows the close match between network-generated and experimentally reconstructed phase maps. The network, like in the case of the optical waveguide dataset, predicts that the phase map will change with wavelength.

Further, to quantify the performance of MS-QPI+DNN, we performed image quality assessment with SSIM, DSSIM, FSIM, MSE, RMSE, SNR, and PSNR value of two images (the numerically reconstructed and network predicted) corresponding to each wavelength. The SSIM shown between the numerically reconstructed and network-generated results validates the similarity in cell structures for the MG63 cell dataset. The high value of SSIM and FSIM close to 1, signifies that the similarity in structure and feature between the network generated and numerically reconstructed phase maps corresponds to λ=532 nm, λ=633 nm, and λ=808 nm, respectively. The phase map comparison results and the image quality assessment values between numerically reconstructed and network generated phase maps signify that the proposed MS-QPI+DNN framework is trained for MS-QPI with a higher similarity in structure, feature and good quality with minimum error for multi-spectral phase map data generation. To show the difference between the reconstructed image and the network output image more directly, a one-dimensional plot of the same area for comparison is provided in the **Supplementary Figure 8**. In support of the network performance, the histogram plot of MSE, SSIM and PSNR over the complete test dataset, few more reconstructed results and quantifying parameters are provided in the **Supplementary Figure 4, 5 and 6** on the **Supplement file 2.**

Table. 1 Time comparison between conventional and proposed DL based MS-QPI method

System Specification	**Time required for reconstruction in conventional MS-QPI**	**Time required in MS-QPI+DNN framework**
NVIDIA DGX-A100 server (AMD EPYC 7742 CPU, NVIDIA A100 40GB GPU)	**3348.48ms ± 0.7657** per run (mean ± std. dev. of 10 runs)	a. Training time (time for 100 epochs): (Batch Size 1): 27.76 hours b. Inference time: **108ms ± 26.3ms** per run (mean ± std. dev. of 10 runs)

In addition, we compared the conventional imaging method (FT+TIE) with our proposed DL based single-shot MS-QPI. Interestingly, our presented MS-QPI+DNN framework provides 31X of significant time reduction from the conventional imaging platform as shown in Table 1.

7. Conclusion

In the present manuscript, we have demonstrated a partially spatially coherent (PSC) light-based single shot multi-spectral quantitative phase imaging (MS-QPI) technique assisted by a deep neural network (DNN). A trained DNN is used to generate three multi spectral phase maps corresponding to λ=532 nm (green), λ=633 nm (red), and λ=808 nm (NIR) from a single input interferogram (λ=633 nm (red)). Initially, we only used two wavelength datasets for the optical waveguide, green and red, to validate our method. Following the successful adaption of the network with two wavelengths for the optical waveguide, we used three wavelengths i.e., green, red, along with NIR for the biological sample. The performance of the network is tested on the optical waveguide as an industrial object and MG63 osteosarcoma cells as a biological sample. Hence, the proposed approach can be useful for both type of samples.

The comparison results shown in Fig. 4 and 5 indicate that the network generated phase map matches closely with experimentally reconstructed phase maps. To quantify the network performance, image quality assessment is performed with SSIM, DSSIM, FSIM, MSE, RMSE, SNR, and PSNR between the predicted and ground truth images. The errors DSSIM, MSE, and RMSE tending to zero signifies minimum error between the two images and high values of SSIM, FSIM, SNR and PSNR signifies higher similarity in structure, feature and good quality with minimum error for multi-spectral phase map data generation. The proposed deep learning based MSQPI system, overcomes the limitations of traditional MS-QPI approaches and provides significant performance, 3X of significant time reduction along with significant resource and cost reduction management. The present method can be useful for the single shot MS-QPI of biological cells and tissues such as human RBCs and cancer tissues where label-free imaging is important in disease diagnosis and the identification of cancer margins.

Funding

S.B. would like to thank the Council of Scientific & Industrial Research (CSIR), India, Grant/Award Number: 09/086 (1340)-2018EMR-I for financial support of this research work through the research fellowship. K.A. and A.B. would like to thank the European Research Council Starting grant (id 804233) and the INTPART grant (id 309802).

Acknowledgement

SB and AB contributed equally to this work. The MS-QPI+DNN framework was developed by SB and AB. SB, AK, and PT acquired the optical waveguide and MG63 osteosarcoma cell datasets. Under the supervision of NS, the cell culturing and storing are done by AJ. The training parameters and performance evaluation of the GAN architecture are optimised by SB in close collaboration with AB, SJ and DKP. SB, AK, and AB wrote the first draft of the manuscript, and other authors contributed to its completion. The authors would also like to thank Dibakar Borah, "MTech Applied Optics, IIT Delhi, India," for his contribution to the manuscript. The entire work is supervised by KA and DSM.

Disclosures

The authors declare no conflict of interest.

Supplemental document

See **supplement 1** and **supplement 2** for supporting content.

References

1. G. Popescu, *Quantitative phase imaging of cells and tissues* (McGraw-Hill Education, 2011).

2. G. Popescu, Y. Park, W. Choi, R. R. Dasari, M. S. Feld, and K. Badizadegan, "Imaging red blood cell dynamics by quantitative phase microscopy," Blood Cells, Molecules, Diseases **41**, 10-16 (2008).

3. A. Butola, D. A. Coucheron, K. Szafranska, A. Ahmad, H. Mao, J.-C. Tinguely, P. McCourt, P. Senthilkumaran, D. S. Mehta, and K. Agarwal, "Multimodal on-chip nanoscopy and quantitative phase imaging reveals the nanoscale morphology of liver sinusoidal endothelial cells," Proceedings of the National Academy of Sciences **118**(2021).

4. S. Bhatt, A. Butola, S. R. Kanade, A. Kumar, and D. S. Mehta, "High-resolution single-shot phase-shifting interference microscopy using deep neural network for quantitative phase imaging of biological samples," Journal of Biophotonics, e202000473 (2021).

5. Y. Park, C. Depeursinge, and G. Popescu, "Quantitative phase imaging in biomedicine," Nature Photonics **12**, https://doi.org/10.1038/s41566-018-0253-x, 578-589 (2018).

6. K. Lee, K. Kim, J. Jung, J. Heo, S. Cho, S. Lee, G. Chang, Y. Jo, H. Park, and Y. Park, "Quantitative Phase Imaging Techniques for the Study of Cell Pathophysiology: From Principles to Applications," **13**, https://www.mdpi.com/1424-8220/13/4/4170, 4170-4191 (2013).

7. A. Butola, D. Popova, D. K. Prasad, A. Ahmad, A. Habib, J. C. Tinguely, P. Basnet, G. Acharya, P. Senthilkumaran, and D. S. Mehta, "High spatially sensitive quantitative phase imaging assisted with deep neural network for classification of human spermatozoa under stressed condition," Scientific reports **10**, 1-12 (2020).

8. S. Bhatt, A. Butola, S. R. Kanade, A. Kumar, and D. S. Mehta, "Single-shot phase-shifting interferometry using deep learning," in *European Conference on Biomedical Optics*, (Optical Society of America, 2021), ETu2A. 51.

9. Y. Rivenson, Y. Zhang, H. Günaydın, D. Teng, and A. Ozcan, "Phase recovery and holographic image reconstruction using deep learning in neural networks," Light: Science Applications 7, 17141-17141 (2018).

10. K. Wang, J. Di, Y. Li, Z. Ren, Q. Kemao, and J. Zhao, "Transport of intensity equation from a single intensity image via deep learning," Optics Lasers in Engineering 134, 106233 (2020).

11. N. Yoneda, A. Onishi, Y. Saita, K. Komuro, and T. Nomura, "Single-shot higher-order transport-of-intensity quantitative phase imaging based on computer-generated holography," Optics Express 29, 4783-4801 (2021).

12. M. Rubin, G. Dardikman, S. K. Mirsky, N. A. Turko, and N. T. Shaked, "Six-pack off-axis holography," Opt. Lett. 42, 4611-4614 (2017).

13. M. H. Jenkins and T. K. Gaylord, "Three-dimensional quantitative phase imaging via tomographic deconvolution phase microscopy," Applied optics **54**, 9213-9227 (2015).

14. Y. Sung, W. Choi, C. Fang-Yen, K. Badizadegan, R. R. Dasari, and M. S. Feld, "Optical diffraction tomography for high resolution live cell imaging," Optics express **17**, 266-277 (2009).

15. S. L. Jacques and Biology, "Optical properties of biological tissues: a review," Physics in Medicine **58**, R37 (2013).

16. G. Popescu, T. Ikeda, R. R. Dasari, and M. S. Feld, "Diffraction phase microscopy for quantifying cell structure and dynamics," Optics letters **31**, 775-777 (2006).

17. B. Bhaduri, H. Pham, M. Mir, and G. Popescu, "Diffraction phase microscopy with white light," Optics letters **37**, 1094-1096 (2012).

18. D. Fu, W. Choi, Y. Sung, Z. Yaqoob, R. R. Dasari, and M. Feld, "Quantitative dispersion microscopy," Biomedical optics express **1**, 347-353 (2010).

19. M. Rinehart, Y. Zhu, and A. Wax, "Quantitative phase spectroscopy," Biomedical optics express **3**, 958-965 (2012).

20. Y. Jang, J. Jang, and Y. Park, "Dynamic spectroscopic phase microscopy for quantifying hemoglobin concentration and dynamic membrane fluctuation in red blood cells," Optics express **20**, 9673-9681 (2012).

21. J.-H. Jung, J. Jang, and Y. Park, "Spectro-refractometry of individual microscopic objects using swept-source quantitative phase imaging," Analytical chemistry **85**, 10519-10525 (2013).

22. V. Dubey, G. Singh, V. Singh, A. Ahmad, and D. S. Mehta, "Multispectral quantitative phase imaging of human red blood cells using inexpensive narrowband multicolor LEDs," Applied optics **55**, 2521-2525 (2016).

23. A. Machikhin, O. Polschikova, A. Ramazanova, and V. Pozhar, "Multi-spectral quantitative phase imaging based on filtration of light via ultrasonic wave," Journal of Optics **19**, 075301 (2017).

24. U. P. Kumar, B. Bhaduri, M. Kothiyal, and N. K. Mohan, "Two-wavelength micro-interferometry for 3-D surface profiling," Optics Lasers in Engineering **47**, 223-229 (2009).

25. V. Singh, R. Joshi, S. Tayal, and D. S. Mehta, "Speckle-free common-path quantitative phase imaging with high temporal phase stability using a partially spatially coherent multi-spectral light source," Laser Physics Letters **16**, 025601 (2019).

26. A. Ahmad, "Development of highly stable and sensitive quantitative phase microscopy and tomography," 2018).

27. D. Singh Mehta and V. Srivastava, "Quantitative phase imaging of human red blood cells using phase-shifting white light interference microscopy with colour fringe analysis," Applied Physics Letters **101**, 203701 (2012).

28. A. Pförtner and J. Schwider, "Red-green-blue interferometer for the metrology of discontinuous structures," Applied optics **42**, 667-673 (2003).

29. A. S. Machikhin, O. V. Polschikova, A. G. Vlasova, and V. E. Pozhar, "Processing of three-wavelength interference pattern for single-shot quantitative phase imaging," in *Twelfth International Conference on Digital Image Processing (ICDIP 2020)*, (SPIE, 2020), 294-298.

30. S. Bhatt, A. Butola, P. Thapa, A. Saxena, A. Ahmad, and D. S. Mehta, "Partially Spatially Coherent Light-Based Multispectral Quantitative Phase Microscopy," in *Optics and the Brain*, (Optica Publishing Group, 2022), JTu3A. 19.

31. K. Dijkstra, J. van de Loosdrecht, L. R. Schomaker, and M. A. Wiering, "Hyperspectral demosaicking and crosstalk correction using deep learning," Machine Vision Applications **30**, 1-21 (2019).

32. Y. Ye, H. Li, G. Li, and L. Lin, "A crosstalk correction method to improve multi-wavelength LEDs imaging quality based on color camera and frame accumulation," Signal Processing: Image Communication **102**, 116624 (2022).

33. A. Serafetinides, M. Makropoulou, and E. Drakaki, "Biophotonics in diagnosis and modeling of tissue pathologies," in *15th International School on Quantum Electronics: Laser Physics and Applications*, (SPIE, 2008), 355-369.

34. P. K. Upputuri and M. Pramanik, "Photoacoustic imaging in the second near-infrared window: a review," Journal of biomedical optics **24**, 040901 (2019).

35. A. Vogel and V. Venugopalan, "Mechanisms of pulsed laser ablation of biological tissues," Chemical reviews **103**, 577-644 (2003).

36. W.-F. Cheong, S. A. Prahl, and A. J. Welch, "A review of the optical properties of biological tissues," IEEE journal of quantum electronics **26**, 2166-2185 (1990).

37. D. S. Mehta, D. N. Naik, R. K. Singh, and M. Takeda, "Laser speckle reduction by multimode optical fiber bundle with combined temporal, spatial, and angular diversity," Applied optics **51**, 1894-1904 (2012).

38. J. W. Goodman, "Statistical properties of laser speckle patterns," in *Laser speckle and related phenomena* (Springer, 1975), pp. 9-75.

39. A. Safrani and I. Abdulhalim, "Ultrahigh-resolution full-field optical coherence tomography using spatial coherence gating and quasi-monochromatic illumination," Optics letters **37**, 458-460 (2012).

40. D. Paganin and K. A. Nugent, "Noninterferometric phase imaging with partially coherent light," Physical review letters **80**, 2586 (1998).

41. N. Pandey, A. Ghosh, and K. Khare, "Two-dimensional phase unwrapping using the transport of intensity equation," Applied optics **55**, 2418-2425 (2016).

42. Y. W. Hu Jason, Yu Zhouchangwan, "Image-to-Image Translation with Conditional-GAN," https://cs230.stanford.edu/projects_spring_2018/reports/8289557.pdf.

43. O. Ronneberger, P. Fischer, and T. Brox, "U-net: Convolutional networks for biomedical image segmentation," in *International Conference on Medical image computing and computer-assisted intervention*, (Springer, 2015), 234-241.

44. P. Isola, J.-Y. Zhu, T. Zhou, and A. A. Efros, "Image-to-image translation with conditional adversarial networks," in *Proceedings of the IEEE conference on computer vision and pattern recognition*, 2017), 1125-1134.

45. I. Goodfellow, J. Pouget-Abadie, M. Mirza, B. Xu, D. Warde-Farley, S. Ozair, A. Courville, and Y. Bengio, "Generative adversarial nets," Advances in neural information processing systems **27**(2014).

46. Z. Wang, A. C. Bovik, H. R. Sheikh, and E. P. Simoncelli, "Image quality assessment: from error visibility to structural similarity," IEEE transactions on image processing **13**, 600-612 (2004).

47. U. Sara, M. Akter, and M. S. Uddin, "Image quality assessment through FSIM, SSIM, MSE and PSNR—a comparative study," Journal of Computer Communications 7, 8-18 (2019).

48. X. Zhang, S. Bloch, W. Akers, and S. Achilefu, "Near-infrared molecular probes for in vivo imaging," Current protocols in cytometry **60**, 12.27. 11-12.27. 20 (2012).